Spectroscopic neutron imaging for resolving hydrogen dynamics changes in battery electrolytes

Author(s):
Carreón Ruiz, E. Riccardo; Lee, Jongmin; Márquez Damián, J. Ignacio; Strobl, Markus; Burca, Genoveva; Woracek, Robin; Ebert, Marc-Olivier; Winter, Eric; Cochet, Magali; Höltschi, Laura; Kadletz, Peter M.; Zlobinski, Mateusz; Tremsin, Anton S.; Gubler, Lorenz; Boillat, Pierre

Publication date:
2023-08

Permanent link:
https://doi.org/https://doi.org/10.3929/ethz-b-000626586

Originally published in:
Materials Today Advances 19, https://doi.org/10.1016/j.mtadv.2023.100405

Materials Today Advances 19 (2023) 100405

Contents lists available at ScienceDirect

Materials Today Advances

journal homepage: www.journals.elsevier.com/materials-today-advances/

Spectroscopic neutron imaging for resolving hydrogen dynamics changes in battery electrolytes

E. Ricardo Carreón Ruiz [a], Jongmin Lee [a, b], J. Ignacio Márquez Damián [c], Markus Strobl [b, d], Genoveva Burca [e, f], Robin Woracek [g], Marc-Olivier Ebert [h], Eric Winter [a], Magali Cochet [a], Laura Höltschi [a], Peter M. Kadletz [g], Mateusz Zlobinski [a], Anton S. Tremsin [i], Lorenz Gubler [a], Pierre Boillat [a, b, *]

[a] Electrochemistry Laboratory (LEC), Paul Scherrer Institut (PSI), 5232, Villigen PSI, Switzerland
[b] Laboratory for Neutron Scattering and Imaging (LNS), Paul Scherrer Institut (PSI), 5232, Villigen PSI, Switzerland
[c] Spallation Physics Group, European Spallation Source ERIC, P.O. Box 176, 22100, Lund, Sweden
[d] Niels Bohr Institute, University of Copenhagen, Nørregade 10, 1165, Copenhagen, Denmark
[e] STFC-Rutherford Appleton Laboratory, ISIS Facility, Harwell, OX11 0QX, UK
[f] Faculty of Science and Engineering, The University of Manchester, Alan Turing Building, Oxford Road, Manchester, M13 9PL, UK
[g] European Spallation Source ERIC, P.O. Box 176, 22100, Lund, Sweden
[h] Department of Chemistry and Applied Biosciences, ETH Zurich, Vladimir-Prelog-Weg 1-5, 8093, Zurich, Switzerland
[i] Space Sciences Laboratory, University of California, Berkeley, CA, 94720, USA

ARTICLE INFO

Article history:
Received 4 June 2023
Received in revised form
26 June 2023
Accepted 26 June 2023
Available online 15 July 2023

Keywords:
Non-destructive characterization
Battery organic solvents
Wavelength-resolved imaging
Neutron radiography
Lithium-ion electrolyte materials

ABSTRACT

We present the use of spectroscopic neutron imaging (SNI), a bridge between imaging and scattering techniques, for analyzing battery electrolytes. The scattering information of CH_n—based organic solvents and electrolytes was mapped in a two-dimensional space through time-of-flight neutron imaging, which exploits the wavelength-dependent properties of hydrogen atoms. The results show partial solidification and concertation change of electrolyte as a function of temperature. Our investigation demonstrates a novel approach to tracking real-time physical and chemical changes in H-containing compounds, by which limitations of new electrolyte mixtures and additives can be evaluated. The sensitivity of SNI to hydrogen in CH_n functional groups extends the use of spectral methods to inspect electrolytes in Li-ion batteries and organic solvents for relevant applications beyond electrochemical systems.

1. Introduction

Capabilities of neutron imaging (NI) have been significantly expanded with the advent of energy-resolved neutron imaging, which has become an essential tool for non-destructive material characterization [1–5], including studies of electrochemical energy storage and conversion devices [6,7]. The particular advantage of NI to investigate light elements of technological importance, i.e., hydrogen and lithium, even in *operando* processes has contributed to the improvements of green mobility technologies such as fuel cells [8,9] and lithium-ion batteries [10] (LIBs).

Electrodes in LIBs have been extensively studied by conventional (white-beam) NI [11–15], and energy-resolved NI has been effective in determining the state-of-charge via Bragg-edge analysis [16,17]. Physical or chemical changes in the electrolytes, on the other hand, are typically studied using spectroscopic techniques including Raman, nuclear magnetic resonance, and Fourier-transform infrared spectroscopies [18–22]. However, these techniques usually require specifically designed cells or involve complicated procedures to extract the electrolytes. Therefore, it is common to perform *post-mortem* mimicking *operando* conditions.

Neutron instrumentation development (detection systems [3,23–26], methods [2,27,28]) narrowed the gap [29,30] between information accessible by imaging and scattering techniques [31–33], which lead to the design of new beamlines (e.g., ODIN, ESS [31]) to exploit new opportunities, especially in the NI field. In this work, we demonstrate that a study of battery electrolytes

* Corresponding author. Electrochemistry Laboratory (LEC), Paul Scherrer Institut (PSI), 5232, Villigen PSI, Switzerland.
E-mail address: pierre.boillate@psi.ch (P. Boillat).

https://doi.org/10.1016/j.mtadv.2023.100405

(particularly liquid organic solvents) has become feasible with spectral techniques as time-of-flight (ToF) NI, and we present an approach to extend it towards a spectroscopic method to resolve physical and chemical changes by analyzing the H total attenuation cross-section. We aim to develop a methodology to study hydrogenated molecules in lithium-ion battery electrolytes *ex situ* and *in situ*.

1.1. Theory: bridging the gap between neutron imaging and spectroscopy

NI techniques are based on neutron interaction with matter, which is described by the Beer-Lambert law, $T = e^{-\Sigma\delta}$, where T is the transmission, δ is the path length, and Σ is the attenuation coefficient of the material. While conventional NI is performed with a polychromatic neutron beam (no energy selection), energy-resolved NI is performed with monochromators or the ToF method, which requires the use of pulsed sources or chopper disks that facilitate the spread of neutrons in time according to their energy. The speed of neutrons is proportional to the square root of their energy (E), whose equivalence to the wavelength (λ) is given by the de Broglie relation, $\lambda = \mathrm{h}/\sqrt{2m_nE}$ [34], where h is the Planck constant, and m_n is the neutron mass. Attenuation coefficients are related to the number density, N_i, of nuclei in the sample and the neutron total cross-section $\sigma_T(\lambda)$. The $\sigma_T(\lambda)$ is the sum of the absorption $\sigma_a(\lambda)$, coherent $\sigma_{coh}(\lambda)$, and incoherent $\sigma_{inc}(\lambda)$ scattering cross-sections, and they are energy-dependent for each atom [35], compound [36,37], and intramolecular bonds [38].

In material science and condensed matter research, dynamic processes are studied by inelastic neutron scattering (INS) and quasi-elastic neutron scattering (QENS), which take advantage of the large $\sigma_{inc}(\lambda)$ contribution of ^{1}H [39–41]. The quantity measured in QENS experiments is the double differential scattering cross-section (DDSCS), $\frac{\partial^2\sigma}{\partial\Omega\partial\lambda'} = \frac{k_f}{k_i}\left\{\frac{\sigma_{coh}}{4\pi}S_{coh}(\alpha,\beta) + \frac{\sigma_{inc}}{4\pi}S_{inc}(\alpha,\beta)\right\}$, where k_i is the wavenumber of the incident neutrons and k_f is the wavenumber of the scattered neutrons, S is the coherent and incoherent coefficient in the thermal scattering law [38,41,42], and α and β are momentum and energy transfer variables, respectively [42,43]. The scattering cross-section, $\sigma_{sct}(\lambda)$, and therefore the N_i of nuclei $(\sigma_{coh}(\lambda) + \sigma_{inc}(\lambda))$, is calculated from the DDSCS, $\sigma_{sct}(\lambda) = \iint\frac{\partial^2\sigma}{\partial\Omega\partial\lambda'}\partial\lambda'\partial\Omega$ [42].

In protonated organic molecules, such as solvents used in Li-ion cells, the main contribution to the signal derives from the ^{1}H incoherent scattering cross-section (coherent cross-section: 1.76 barns and incoherent cross-section: 80.26 barns) [43–45]. The remaining elements, i.e., carbon and oxygen, have a negligible incoherent scattering cross-section (0.0010 barns and 0.0008 barns, respectively), and in this study, their contributions were corrected by subtracting the corresponding free atom scattering cross-section (5.551 barns and 4.232 barns, respectively) [46] to obtain just the σ_T^{mol} of the molecule, i.e., $\sigma_T^{mol} = A\sigma_T^C + B\sigma_T^O + C\sigma_T^H$, where A, B, and C are the number of atoms in the molecule, respectively. This process is similar to the average functional group approximation, described by Romanelli et al. [38]. With these considerations, a transmission image T includes the elastic and inelastic components of the incoherent scattering process $(S_{inc}^{el}(\alpha) + S_{inc}^{inel}(\alpha,\beta))$. The elastic incoherent part carries information about the quantity and type of scattering atoms. On the other hand, the inelastic component provides information on the motion of these atoms, due to molecular vibration or diffusion processes. In this way, and by applying the Beer-Lambert law to calculate the ^{1}H total neutron attenuation cross-section, $\sigma_T^H(\lambda)$, we exploit for the first time that transmission images obtained by ToF-NI provide spatially resolved information on the chemical and physical properties of organic materials. The fully non-invasive aspect of neutron imaging allows investigating electrolyte degradation and/or physical changes within real systems (i.e., while confined in metallic casings), which is crucial to understanding performance limitations in LIBs.

2. Materials and methods

Two sets of experiments were performed at two neutron facilities: a reactor neutron source (V20 ESS test-beamline at HZB in Berlin) [32], where the physical pulses were generated with a chopper system, and a pulsed spallation source (IMAT beamline of ISIS RAL in the UK) [47]. The first experiment (V20) was performed with organic solvents and electrolytes enclosed in empty coin cell casings in a through-plane setup at a wavelength range of 1.50 Å to 9.6 Å. The total exposure time for each sample batch (two coin cells at the same time) was fixed to 2 h with 5-min ToF imaging cycles. The second experiment (IMAT) was conducted with two wavelength ranges, 0.7–6.5 Å, and 3.5–9.7 Å. The total exposure time was fixed to 3 h and 1 h, respectively, per sample batch (four cuvettes at the same time) with 5-min ToF imaging cycles. To probe the transmission of organic solvents and electrolytes and to calculate the $\sigma_T^H(\lambda)$, we used a stainless steel holder including 16 cuvettes of 3 mm thickness to optimize the utilization of the limited field-of-view (FoV) in the detector. A micro-channel plate (MCP) detector [48] with a 28 × 28mm 2 FoV and 55 μm pixel size in normal transmission geometry was used for both measurements.

During the experiment, the sample-detector distance was 8 ± 0.5 mm, i.e., total distance taking into account the sample holder thickness. The main advantage of utilizing the pulsed beam at IMAT beamline with an MCP detector is that, during time-of-flight, the detector generates frames (456 frames per acquisition in a 5 Hz pulse ranging from 0.7 to 6.5 Å) of each time-of-flight arriving point, that is then a monochromatic beam with an approximate Δλ = 0.4Å. Therefore, no beam hardening is observed. The images obtained with an MCP detector are not significantly affected by background scattering (SBKG). To further improve data accuracy, the SBKG was computed by interplating regions among 5-mm-thick Cd black body (BB) stripes at the bottom, top, and top border of the FoV. The SBKG correction was applied to each frame-wise image [49]. To account for intensity fluctuations of the beam throughout the experiment, the area between the last set of BBs was defined as a non-changing region (open beam within the sample in the FoV). By comparing these regions in the reference (empty sample holder –ref-) and the hydrogenous sample (filled sample holder –img-), the intensity of each image was corrected. The MCP detector performs identically for both img and ref. Thus, we measure a relative transmission, T, with a constant wavelength efficiency throughout the experiment.

Two sources of error are identified, systematic and statistical. The latter takes into account the statistical variation among acquisitions: the evaluation time (5 min per acquisition), the total exposure time (36 acquisitions for a total of 3 h for wavelengths in between 0.7 and 6.5 Å and 12 acquisitions -1 h-for 3.5–9.7 Å), and the region of interest selected (smallest area taken for solidified species 24 × 54 pixels ≈ 71 mm^2). The statistical variation was calculated using a 99% confidence interval with Student's t-values for evaluating the margin of error $(t(n-1)/\sqrt{n})$, where n is the number of images for a fixed exposure time. For a total of 3 h exposure time, we estimated 0.21%, and for 1 h 0.32% of variation. Hereby, we confirm that the most substantial deviation derives from systematic errors, which is less than 2% as Fig. 1-inset shows.

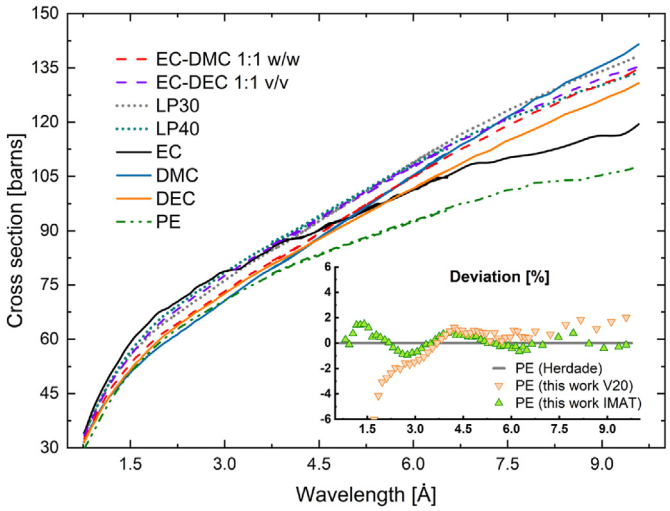

Fig. 1. Calculated $\sigma_T^H(\lambda)$ in organic solvents, organic binary mixtures, and electrolytes (IMAT beamline). Cross-section dependence on the nature of the molecule to which H is bonded. Inset: percentage deviation between calculations of $\sigma_T^H(\lambda)$ in polyethylene in our experiments, as reference material, compared to literature data [36,37].

The samples consist of pure organic solvents from BASF and Sigma Aldrich: ethylene carbonate (EC), dimethyl carbonate (DMC), and diethyl carbonate (DEC). Organic binary mixtures: EC-DMC 1:1 w/w, EC-DEC 1:1 v/v, and EC-DEC 3:7 v/v. Electrolytes: LP30 (1 M $LiPF_6$ in EC-DMC 1:1 w/w), LP40 (1 M $LiPF_6$ in EC-DEC 1:1 v/v), LP47 (1 M $LiPF_6$ in EC-DEC 3:7 w/w). The CH_n bonds included in each organic molecule are: two CH_2 bonds in EC, two CH_3 bonds in DMC, and one pair of CH_2 and CH_3 bonds in DEC. A comparison between IMAT and V20 cross-section results can be found in the supplementary material section (appendix-A).

3. Results and discussion

The calculation of the $\sigma_T^H(\lambda)$ from transmission images in ToF-NI experiments (Fig. 1) revealed variations in the ^1H scattering behavior in different compounds. A good agreement was found between our measurements of ^1H in polyethylene (PE), as reference material, and literature data with an error below 1.5% (at the IMAT) shown in Fig. 1 downright. The natural fluctuation of $\sigma_T^H(\lambda)$ results in a wavelength-dependent distinction between organic materials, based on the atomic bonds, intermolecular interactions, and the overall dynamic characteristics of each molecule including diffusion.

The curves shown in Fig. 1 are a rater complex convolution of molecular dynamic features that are not easily discerned, which is the fundamental reason to use simulations. In our approach, we associate simulations and measurements to identify the contributions that cause the fine variations in the curves. Therefore, to accentuate said divergence, the $\sigma_T^H(\lambda)$ of each sample was normalized to that of PE reference (EXFOR) and divided by its cross-section value at 3 Å (Fig. 2-a). At short λ (< 3 Å), H cross-sections provide information of the overall vibrational features of the molecule. Molecules with the same vibrational modes overlap, i.e., CH_2-rich molecules on top, molecules with a combination of CH_2-rich and CH_3 molecules in the middle, pure molecules containing a balanced combination of CH_2 and CH_3 at the bottom, and molecules containing pure CH_3 diverging along the region. Thus, a separation between CH_n (especially between CH_2 and CH_3) functional groups can be observed (Fig. 2-a inset). A similar analysis was performed at

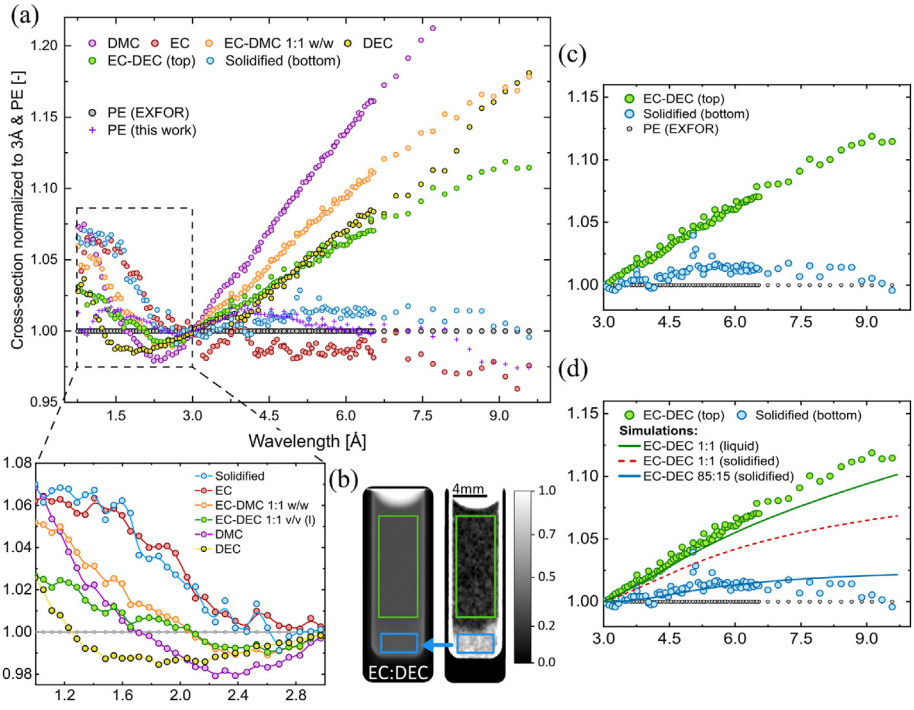

Fig. 2. Partial solidification of an organic binary mixture. (a) ^1H cross-sections normalized to PE (EXFOR) at 3 Å: Liquid binary mixtures (EC-DEC 1:1 v/v and EC-DMC 1:1 w/w) and pure organic solvents (EC and DMC). Region $1 < \lambda < 3$ Å (inset) shows differences among solvents according to their overall molecular vibration. The fine variations depend on the aggregation state of the sample and chemical structure (H fraction in CHn groups). (b) Cut off of the cuvette neutron radiograph presenting a partial solidification at 3 Å (left) and adjustment of the contrast (right) focused on the solid deposit. Green and blue regions were used in the calculation of the $\sigma_T^H(\lambda)$ for each component. (c) Long wavelength region of the experimental data points of the cuvette presented in (b). (d) Simulation of the solid deposit (EC-enriched), the liquid organic binary solvent (DEC-enriched), and the case where no concentration change would occur (EC-DEC 1:1 v/v). (For interpretation of the references to colour in this figure legend, the reader is referred to the Web version of this article.)

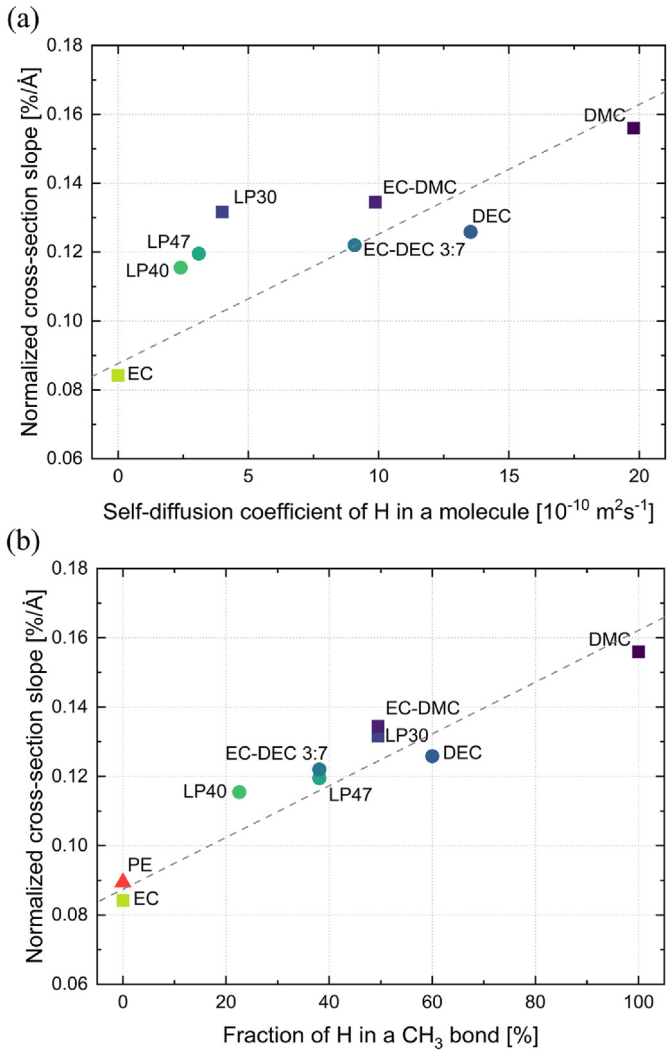

Fig. 3. Relationship between the $\sigma_T^H(\lambda)$ **normalized slope and** (a) the measured 1H self-diffusion coefficients of pure organic solvents, organic binary mixtures, and electrolytes. (b) the fraction of H in CH3 bonds in each molecule. Squared markers represent solvents whose individual molecules contain pure CH2 (EC), CH3 (DMC) or a pure combination of CH2 and CH3 (EC-DMC) functional groups, circular markers represent individual molecules with both CH2 and CH3 functional groups, such as DEC.

long λ (> 3 Å), where the change is even more substantial and additional information about a concentration change of a molecule can be obtained. In both short and long λ regions, information about the aggregation state of the sample can be found. The evidence of this particular behavior along the spectrum originated from the observation of a partial solidification at experiment temperature (290 K) (Fig. 2-b) in an organic binary solvent (EC-DEC 1:1 v/v), which is the base of the LP40 electrolyte (1 M $LiPF_6$ in EC-DEC 1:1 v/v). The radiograph revealed a deposit at the bottom of the cuvette with a different transmission signal than that of the top part. The contrast variation is attributed either to the presence of solid EC or to a solid mixture containing high EC concentration. The phase change and the solid aggregation state of the deposit were confirmed considering the curve has a comparable behavior as EC (melting point 312 K) in both the vibrational and diffusion regions.

The significant difference of $\sigma_T^H(\lambda)$ between the liquid and solid curves in the diffusion region are due to the solidification (phase change effect), a change of composition (mixture EC-DEC with an EC enrichment, a concentration change effect), or both. A $\sigma_T^H(\lambda)$ simulation (appendix-B) of this solvent (dashed red curve in Fig. 2-a), where the self-diffusion coefficient is set to zero, i.e., assuming solidification of EC-DEC 1:1 v/v without changing concentrations, indicates that a reduction of the slope in the diffusion region of the material is expected. However, it is rather small compared to our observations. From the phase diagram of the mixture EC-DEC [50], the co-existence of a solid EC phase with an EC-depleted liquid phase is expected at 290 K. Therefore, a simulation of this component in the solid state with a higher EC concentration (85:15) was performed. The blue curve in Fig. 2-a mimics the change of concentration and shows a better fit to the slope reduction observed experimentally indicating both the change of concentration and the phase transition to the solid state of the sample. The major part of the slope reduction in our measurements is caused by the separation of an EC-enriched solid deposit, which was accumulated at the bottom of the sample.

To analyze the relationship between $\sigma_T^H(\lambda)$ at long λ and the properties of the molecule, like viscosity, the slope of the normalized cross-sections in the diffusion region ($\lambda >$ 3 Å) was calculated. In addition, the H self-diffusion coefficients of all samples were measured at 290 K by NMR spectroscopy, by which the binary diffusion coefficients of organic binary mixtures and electrolytes were calculated. Fig. 3-a shows, as a first hypothesis, the relationship between the $\sigma_T^H(\lambda)$ slope values at long λ with the diffusion coefficients. One should expect a distinction in the slope of molecules with substantially different mobility, i.e., the binary mixture EC-DEC 3:7 and the electrolyte LP47. However, this is true only for pure solvents (EC, DEC, and DMC). This fact suggests that the $\sigma_T^H(\lambda)$ slope is not that much influenced by the H self-diffusion, but rather by the type of chemical bond, as confirmed by our simulations. Particularly, the slope takes into account the nature and fraction of CH_2 and CH_3 in each molecule, i.e., DEC contains a combination of both CH_2 and CH_3 functional groups (circular markers) in contrast to pure and combinations of pure CH_n functional groups (squared markers). A confirmation of this hypothesis is observed in Fig. 3-b, where the molar fraction of H in CH_3 bonds was calculated for each sample. Here, a stronger correlation between the normalized $\sigma_T^H(\lambda)$ slope and the fraction of H in CH_3 functional groups are shown.

The slope at long λ due to relatively small molecules containing only CH_3 bonds, such as DMC, provide a higher value of $\sigma_T^H(\lambda)$ than that of larger molecules containing both CH_3 and CH_2 bonds, such as DEC. Romanelli et al. [38] observed similar behavior in the same energy range when determining $\sigma_T(\lambda)$ of amino acids at ISIS-VESUVIO neutron spectrometer. They explain that the higher value of $\sigma_T(\lambda)$ in CH_3 bonds is due to low-energy excitation and de-excitations in its vibrational density of states (VDoS), which fits within numerical accuracy for $\sigma_T^H(\lambda)$ in the case of CH, CH_2, and CH_3 molecules. The results provided by the spectroscopic neutron imaging (SNI) method confirm the unique characteristic of ToF-NI to identify spectroscopic information in 2D real-time space, especially for CH_n functional groups.

The $\sigma_T^H(\lambda)$ slope is a simple approach to investigating changes in electrolytes. Still, examining the full spectra (Fig. 2) provides more opportunities for identifying overall changes, e.g., while the difference of slopes at long λ between DEC and EC-DEC 3:7, is imperceptible, the information provided by the vibrational region (low λ) shows a considerable contrasting behavior, due to unique features of each molecule.

The substantial signal change in $\sigma_T^H(\lambda)$ due to physical changes and intrinsic molecular dynamics perceived along the thermal-to-cold neutron energies (0.6 Å to 9 Å) constitutes a fundamental strength of the method in addition to its spatially resolved nature. The results obtained in this experiment demonstrate the use of ToF-

NI as a spectroscopic method to track phase changes and to differentiate specific organic molecules based on the nature of their bonds. These attributes are crucial to applications in material science and especially in the investigation of electrolyte degradation in LIBs, where the direct study of physico-chemical reactions occurring inside metal casings would otherwise be impossible.

4. Conclusion

In this work, we demonstrate the use of ToF-NI to spatially resolve physico-chemical changes and to obtain spectroscopic information in organic solvents used in LIBs in a non-invasive manner. The images resulting from this technique contain the necessary information to track phase and concentration changes, and to differentiate molecules according to their chemical structure.

The study of wavelength-dependent ^{1}H total cross-sections provides insights into understanding the vibration/diffusion dynamics of organic materials and their dependence on the aggregation state (solid or liquid) and the type of CH_n functional groups (e.g., CH_2, CH_3, and combinations). However, based on our measurements and simulations, the latter (type of CH_n groups) has shown a dominant impact compared to the aggregation state.

The wavelength-dependent ^{1}H total cross-sections demonstrate the unique capabilities of ToF-NI as a spatially resolved spectroscopic method. The use of ToF-NI can be applied to a broad range of applications (e.g., Na-ion and Mg-ion based batteries, redox flow batteries) to study *operando* electrolyte degradation, distribution of heterogeneities, partial solidification, and issues related to mass transport mechanisms. The utilization of this method in LIBs for *in situ* tests and *operando* fast-charging protocols will promote the study of performance losses since a correlation between physico-chemical and electrochemical performance is viable.

Credit author statement

E. Ricardo Carreón Ruiz: Writing - original draft, conceptualization, methodology, software, investigation, formal analysis, data curation, visualization, resources. **Jongmin Lee:** Writing - review & editing, supervision, validation. **J. Ignacio Márquez Damián:** Software, validation, formal analysis. **Markus Strobl**: Writing - review & editing, supervision. **Genoveva Burca:** Methodology, investigation. **Robin Woracek:** Methodology, investigation. **Marc-Olivier Ebert:** Resources, investigation. **Eric Winter**: Resources. **Magali Cochet:** Supervision. **Laura Höltschi:** Resources. **Peter M. Kadletz:** Methodology, investigation. **Mateusz Zlobinski:** Investigation. **Anton S. Tremsin:** Methodology. **Lorenz Gubler:** Writing - review & editing, supervision, project administration. **Pierre Boillat**: Writing - review & editing, supervision, software, validation, funding acquisition, project administration.

Data and materials availability

All information required to interpret the conclusions in this work are present in the main text and/or the supplementary materials. The code and raw data from neutron campaigns are available from the corresponding author upon request.

Declaration of competing interest

The authors declare that they have no known competing financial interests or personal relationships that could have appeared to influence the work reported in this paper.

Data availability

Data will be made available on request.

Acknowledgments

The authors would like to thank L. Kondracki, A. Mularczyk, and D. Scheuble for fruitful discussions. We acknowledge financial support from the CROSS initiative and scientific collaboration to the IMAT beamline (experiment RB2000122 with DOI: 10.5286/ISIS.E.RB2000122) at ISIS Neutron and Muon Source (UK) of Science and Technology Facilities Council (STFC).

Appendix A. Supplementary data

Supplementary data to this article can be found online at https://doi.org/10.1016/j.mtadv.2023.100405.

References

[1] N. Kardjilov, I. Manke, A. Hilger, M. Strobl, J. Banhart, Mater. Today 14 (2011) 248–256.
[2] R. Woracek, J. Santisteban, A. Fedrigo, M. Strobl, Nucl. Instrum. Methods Phys. Res.: Accel. Spectrom. Detect. Assoc. Equip. 878 (2018) 141–158.
[3] R. Woracek, M. Krzyzagorski, H. Markötter, P.M. Kadletz, N. Kardjilov, I. Manke, A. Hilger, Opt Express 27 (2019) 26218.
[4] J. Strickland, K. Tassenberg, G. Sheppard, B. Nenchev, S. Perry, J. Li, H. Dong, G. Burca, J. Kelleher, S. Irwin, Sci. Rep. 10 (2020) 20751.
[5] K.V. Tran, R. Woracek, N. Kardjilov, H. Markötter, A. Hilger, W. Kockelmann, J. Kelleher, S.B. Puplampu, D. Penumadu, A.S. Tremsin, J. Banhart, I. Manke, Mater. Today Adv. 9 (2021) 100132.
[6] M. Siegwart, R. Woracek, J.I. Márquez Damián, A.S. Tremsin, V. Manzi-Orezzoli, M. Strobl, T.J. Schmidt, P. Boillat, Rev. Sci. Instrum. 90 (2019) 103705.
[7] J. Biesdorf, P. Oberholzer, F. Bernauer, A. Kaestner, P. Vontobel, E.H. Lehmann, T.J. Schmidt, P. Boillat, Phys. Rev. Lett. 112 (2014) 248301.
[8] A. Forner-Cuenca, J. Biesdorf, V. Manzi-Orezzoli, L. Gubler, T.J. Schmidt, P. Boillat, J. Electrochem. Soc. 163 (2016) F1389–F1398.
[9] V. Manzi-Orezzoli, M. Siegwart, D. Scheuble, T.J. Schmidt, P. Boillat, J. Electrochem. Soc. 167 (2020) 064521.
[10] D. Goers, M. Holzapfel, W. Scheifele, E. Lehmann, P. Vontobel, P. Novák, J. Power Sources 130 (2004) 221–226.
[11] J.P. Owejan, J.J. Gagliardo, S.J. Harris, H. Wang, D.S. Hussey, D.L. Jacobson, Electrochim. Acta 66 (2012) 94–99.
[12] Z. Nie, P. McCormack, H.Z. Bilheux, J.C. Bilheux, J.P. Robinson, J. Nanda, G.M. Koenig, J. Power Sources 419 (2019) 127–136.
[13] H. Zhou, K. An, S. Allu, S. Pannala, J. Li, H.Z. Bilheux, S.K. Martha, J. Nanda, ACS Energy Lett. 1 (2016) 981–986.
[14] J.B. Siegel, X. Lin, A.G. Stefanopoulou, D.S. Hussey, D.L. Jacobson, D. Gorsich, J. Electrochem. Soc. 158 (2011) A523.
[15] N. Kardjilov, I. Manke, R. Woracek, A. Hilger, J. Banhart, Mater. Today 21 (2018) 652–672.
[16] M.-E. Lăcătuşu, L.T. Kuhn, R.E. Johnsen, P.K.M. Tung, S. Schmidt, T. Shinohara, R. Kiyanagi, A.S. Tremsin, N. Elewa, R. Woracek, M. Strobl, arXiv:2104.03564 [cond-mat.mtrl-sci] (2021).
[17] T. Kamiyama, Y. Narita, H. Sato, M. Ohnuma, Y. Kiyanagi, Phys. Procedia 88 (2017) 27–33.
[18] G. Gachot, S. Grugeon, M. Armand, S. Pilard, P. Guenot, J.M. Tarascon, S. Laruelle, J. Power Sources 178 (2008) 409–421.
[19] C.J. Jafta, C. Bridges, L. Haupt, C. Do, P. Sippel, M.J. Cochran, S. Krohns, M. Ohl, A. Loidl, E. Mamontov, P. Lunkenheimer, S. Dai, X.G. Sun, ChemSusChem 11 (2018) 3512–3523.
[20] F. Shi, H. Zhao, G. Liu, P.N. Ross, G.A. Somorjai, K. Komvopoulos, J. Phys. Chem. C 118 (2014) 14732–14738.
[21] K. Hayamizu, Y. Aihara, S. Arai, C. Garcia Martinez, J. Phys. Chem. B103, (1999) 519–524.
[22] S. Laruelle, S. Pilard, P. Guenot, S. Grugeon, J.-M. Tarascon, J. Electrochem. Soc. 151 (2004) A1202.
[23] A.S. Tremsin, J.V. Vallerga, Radiat. Meas. 130 (2020) 106228.
[24] P. Trtik, E.H. Lehmann, J. Phys.: Conf. Ser. 746 (2016) 012004.
[25] N. Borges, A. Losko, S. Vogel, J. Imaging 4 (2018) 40.
[26] A.S. Losko, Y. Han, B. Schillinger, A. Tartaglione, M. Morgano, M. Strobl, J. Long, A.S. Tremsin, M. Schulz, Sci. Rep. 11 (2021) 21360.
[27] M. Strobl, H. Heimonen, S. Schmidt, M. Sales, N. Kardjilov, A. Hilger, I. Manke, T. Shinohara, J. Valsecchi, J. Phys. D Appl. Phys. 52 (2019) 123001.
[28] M. Strobl, R.P. Harti, C. Gruenzweig, R. Woracek, J. Plomp, Journal of Imaging 3 (2017) 64.
[29] E.H. Lehmann, S. Peetermans, P. Trtik, B. Betz, C. Grünzweig, J. Phys.: Conf. Ser. 746 (2017) 012070.
[30] P. Boillat, E.H. Lehmann, P. Trtik, M. Cochet, Curr. Opin. Electrochem. 5 (2017)

3–10.
[31] M. Strobl, Phys. Procedia 69 (2015) 18–26.
[32] R. Woracek, T. Hofmann, M. Bulat, M. Sales, K. Habicht, K. Andersen, M. Strobl, Nucl. Instrum. Methods Phys. Res.: Accel. Spectrom. Det. Assoc. Equip. 839 (2016) 102–116.
[33] R.S. Ramadhan, W. Kockelmann, T. Minniti, B. Chen, D. Parfitt, M.E. Fitzpatrick, A.S. Tremsin, J. Appl. Crystallogr. 52 (2019) 351–368.
[34] A. Dianoux, G. Lander (Eds.), Neutron Data Booklet, Second, OCP Science imprint, Institute Laue-Langevin, Grenoble, 2003.
[35] R.K. Adair, Rev. Mod. Phys. 22 (1950) 249–289.
[36] S.B. Herdade, L.A. Vinhas, C. Rodrigues, Neutron Cross Sections of Polyethylene and Light Water, Instituto de Energia Atomica de Sao Paulo, 1973.
[37] J. Lee, J. Nishiyama, J.-I. Hori, R. Kimura, T. Sako, A. Yamada, T. Sano, J. Nucl. Sci. Technol. 57 (2020) 1–8.
[38] G. Romanelli, D. Onorati, P. Ulpiani, S. Cancelli, E. Perelli-Cippo, J.I. Márquez Damián, S.C. Capelli, G. Croci, A. Muraro, M. Tardocchi, G. Gorini, C. Andreani, R. Senesi, J. Phys. Condens. Matter 33 (2021) 285901.
[39] V.F. Sears, Neutron News 3 (1992) 26–37.
[40] A. Triolo, O. Russina, V. Arrighi, F. Juranyi, S. Janssen, C.M. Gordon, J. Chem. Phys. 119 (2003) 8549–8557.
[41] J.P. Embs, F. Juranyi, R. Hempelmann, Z. Phys. Chem. 224 (2010) 5–32.
[42] Nuclear Energy Agency (NEA), International Evaluation Co-Operation 42 (2020) 60.
[43] K. Ramić, C. Wendorff, Y. Cheng, A.I. Kolesnikov, D.L. Abernathy, L. Daemen, G. Arbanas, L. Leal, Y. Danon, L. (Emily) Liu, Ann. Nucl. Energy 120 (2018) 778–787.
[44] A. Faraone, S. Magazà, R.E. Lechner, S. Longeville, G. Maisano, D. Majolino, P. Migliardo, U. Wanderlingh, J. Chem. Phys. 115 (2001) 3281–3286.
[45] M. Bee, in: PSI-Proceedings 96 (1996) 103–112.
[46] S.C. Capelli, G. Romanelli, J. Appl. Crystallogr. 52 (2019) 1233–1237.
[47] W. Kockelmann, T. Minniti, D.E. Pooley, G. Burca, R. Ramadhan, F.A. Akeroyd, G.D. Howells, C. Moreton-Smith, D.P. Keymer, J. Kelleher, S. Kabra, T. Lik Lee, R. Ziesche, A. Reid, G. Vitucci, G. Gorini, D. Micieli, R.G. Agostino, V. Formoso, F. Aliotta, R. Ponterio, S. Trusso, G. Salvato, C. Vasi, F. Grazzi, K. Watanabe, J.W. L Lee, A.S. Tremsin, J.B. McPhate, D. Nixon, N. Draper, W. Halcrow, J. Nightingale, J. Imaging 4 (2018) 47.
[48] A.S. Tremsin, J.V. Vallerga, J.B. McPhate, O.H.W. Siegmund, R. Raffanti, IEEE Trans. Nucl. Sci. 60 (2013) 578–585.
[49] P. Boillat, C. Carminati, F. Schmid, C. Grünzweig, J. Hovind, A. Kaestner, D. Mannes, M. Morgano, M. Siegwart, P. Trtik, P. Vontobel, E.H. Lehmann, Opt Express 26 (2018) 15769.
[50] M.S. Ding, K. Xu, S. Zhang, T.R. Jow, J. Electrochem. Soc. 148 (2001) A299.